frontiers | Frontiers in Earth Science

TYPE Original Research
PUBLISHED 20 January 2023
DOI 10.3389/feart.2022.1058243

OPEN ACCESS

EDITED BY
Xinjian Shan,
Institute of Geology, China Earthquake Administration, China

REVIEWED BY
Zhongtai He,
Ministry of Emergency Management, China
Dongliang Liu,
Chinese Academy of Geological Sciences (CAGS), China

*CORRESPONDENCE
Lingyun Ji,
jilingyun@smac.ac.cn

SPECIALTY SECTION
This article was submitted to Structural Geology and Tectonics, a section of the journal Frontiers in Earth Science

RECEIVED 30 September 2022
ACCEPTED 29 November 2022
PUBLISHED 20 January 2023

CITATION
Yang C, Ji L, Yang Y, Su L, Wang Y and Shi H (2023), Present-day activity and seismic potential of the north Qinling fault, southern ordos block, central China, as revealed from GPS data and seismicity.
Front. Earth Sci. 10:1058243.
doi: 10.3389/feart.2022.1058243

Present-day activity and seismic potential of the north Qinling fault, southern ordos block, central China, as revealed from GPS data and seismicity

Chenyi Yang[1], Lingyun Ji[2]*, Yihai Yang[1], Lina Su[1], Ying Wang[1] and Huiren Shi[1]

[1]Shaanxi Earthquake Agency, Xi'an, China, [2]The Second Monitoring and Application Center, China Earthquake Administration, Xi'an, China

The North Qinling Fault, located at the boundary of the North China Block and the South China Block, represents an important tectonic structure between the Weihe Basin and the Qinling Mountains, and controls the subsidence and expansion of the Weihe Basin. This fault has been highly active and has caused strong earthquakes since the Holocene and in a pre-seismic stage currently, as indicated by the many paleoearthquake traces found along it. To determine the present-day activity and seismic potential of the North Qinling Fault, by inverting GPS data, we produced fault locking depth, slip rate, and regional strain fields maps; moreover, based on seismicity, we produced a seismic b-value map. Combining this information with modern seismicity, we were able to comprehensively analyze the seismic potential of different fault segments. Our inversion of GPS data showed that the slip rate of the western segment of the fault (Qingjiangkou–Xitangyu) and the correspondent locking depth are 1.33 mm/a and 13.54 km, respectively, while the slip rate of the middle segment (Xitangyu–Fengyukou) and the correspondent locking depth are 0.45 mm/a and 8.58 km, respectively; finally, the slip rate of the eastern segment (Xitangyu–Daiyu) and the correspondent locking depth are 0.36 mm/a and 21.46 km, respectively. The locking depths of the western and middle segments of the fault are shallower than 90% of the seismic cutoff depth, while the locking depth of the eastern segment of the fault is similar to 90% of the seismic cutoff depth, indicating that "deep creep" occurs in the western and middle segments, while the eastern segment is locked. Modern small earthquakes have involved the western and middle segments of the fault, while the eastern segment has acted as a seismic gap with weak seismicity, characterized by a higher shear strain value and a lower b-value. These characteristics reflect the relationship between the locking depth and seismicity distribution. The results of our comprehensive analysis, combined with field geological surveys, show that the eastern segment of the North Qinling Fault has a strong seismic potential and is presently locked.

KEYWORDS

North Qinling Fault, GPS velocity field, locking depth, slip rate, seismicity distribution, seismic potential

1 Introduction

Strong earthquakes (M_S > 7) often occur at the boundary of active blocks in the mainland (Deng et al., 2003; Xu, 2006; Zhang et al., 2013). The North Qinling Fault, an active fault located at the boundary between the North China Block and the South China Block (i.e., first order blocks in Chinese mainland), can produce strong earthquakes (Figure 1). Specifically, the North Qinling Fault lies at the southern boundary of the Weihe Basin, which has been, historically, a strong seismically active area. Three M > 7 earthquakes have been recorded here, the most representative being the 1556 M 8¼ Huaxian earthquake, which caused > 840,000 deaths (https://data.earthquake.cn). Active faults are developed in the basin, among them, the North Qinling Fault is the largest, deepest and the most active fault (Zhang et al., 1990, 1991; Shaanxi Earthquake Agency, 1996; Bai, 2018).

Although there are few records of historical earthquakes along the North Qinling Fault, there are still many traces of ancient earthquakes, landslides, and barrier lakes, implying a number of strong earthquakes should have been caused by this fault since the beginning of the Holocene, demonstrating its earthquake generating ability. Paleoearthquake trenching dating has revealed that strong earthquakes occur about every 3,000 years along the North Qinling Fault, and that we might now be close to the end of the recurrence period: in a pre-seismic stage (Shaanxi Earthquake Agency, 1996; Bai, 2018). Considering these major earthquake hazard conditions, it is ungently needed to study the present-day activity and seismic potential of the North Qinling Fault.

Since the 1980s, detailed studies based on geological exploration have been carried on the North Qinling Fault to understand its geometry, kinematics, dynamics, structural evolution, and seismic ability (Zhang et al., 1990, 1991; Shentu et al., 1991; Bai, 2018; Huang et al., 2020; Yang, 2022). However, previous research has mainly focused on paleoearthquake events and normal faulting along the fault, while, quantitative analyses of the present-day seismic potential associated to current motion (particularly the strike-slip movement of the fault) have not been conducted.

Modern geodetic monitoring (especially GPS monitoring) is an effective and widely method used to recognize ongoing crustal movements. It can be applied to obtain the fault slip rate, locking depth, and strain field, which provide information on the earthquake cycle stage of the fault (Segall and Davis, 1997; Meade and Hager, 2005; Vigny et al., 2005; Papanikolaou et al., 2005; Huang et al., 2019; Chen et al., 2020; Li et al., 2021; Song et al., 2022). Numerous high-resolution analyses of geodetic observations along the active fault have been conducted to identify any

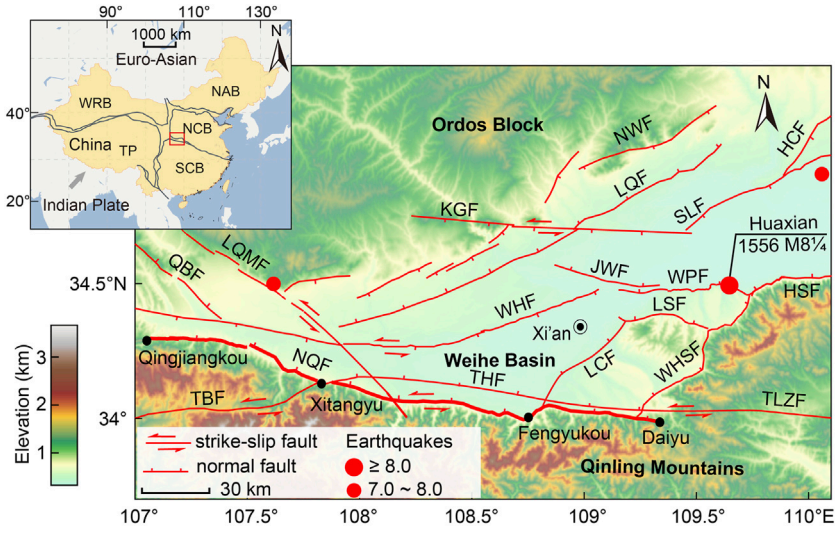

FIGURE 1
Tectonic setting of the North Qinling Fault and of the Weihe Basin. The fault data mainly refer to Deng et al. (2002) and Xu et al. (2016), while the seismic data were obtained from the National Earthquake Data Center (https://data.earthquake.cn). NCB, North China Block; SCB, South China Block; TP, Tibetan Plateau; WRB, Western Region Block; NAB, Northeast Asia Block; NQF, North Qinling Fault; THF, Taochuan–Huxian Fault; TBF, Taibai Fault; TLZF, Tieluzi Fault; LQMF, Longxian–Qishan-Mazhao Fault; QBF, Qianyang–Biaojiao Fault; WHF, Weihe Fault; LCF, Lintong –Chang'an Fault; LSF, Lishan Fault; WHSF, West Huashan Fault; WPF, Weinan Plateau Fault; HSF, Huashan Fault; JWF, Jingyang–Weinan Fault; HCF, Hancheng Fault; SLF, Shuangquan–Linyi Fault; LQF, Liquan Fault; NWF, North Weihe Fault; KGF, Kouzhen–Guanshan Fault.

connections with seismicity distribution and, hence, the current seismotectonic behavior (Sykes, 1971; Perez and Jacob, 1980; Zhang et al., 2003; Becker et al., 2005; Fialko, 2006; Parsons, 2006; Wen et al., 2007, 2008, 2013; Du et al., 2009, 2010, 2018; Wang et al., 2015; Liu et al., 2016; Li et al., 2020; Yin et al., 2020; Zhou et al., 2022).

In this study, we aimed to determine the present-day seismic potential associated with fault strike-slip movement and seismic activity along the North Qinling Fault, based on GPS data and seismicity. Firstly, we divided the North Qinling Fault into three segments from W to E (as in Zhang et al., 1991, Shaanxi Earthquake Agency, 1996 and Bai, 2018), and selected a total of three GPS profiles along the vertical direction of the fault strike (one for each segment). Based on GPS data, we inverted the slip rates, the locking depths, and the strain fields of the segments. Then, we determined any variations in the statistical properties of microseismicity (i.e., b-values and focal depth-frequency), identifying a seismic gap. The earthquake generating capacity of the fault was estimated by calculating the moment magnitude. Finally, we discussed the present-day activity and the seismic potential of the North Qinling Fault segments. The outcome of this study is vital to assess the seismic hazards and earthquake prediction in the densely populated Weihe Basin.

2 Geological setting

The North Qinling Fault is located in the northeastern part of the Tibetan Plateau, at the southern Ordos Block, central China (Figure 1). This fault formed due to multi-stage tectonic movements, which controlled the subsidence and evolution of the Weihe Basin to the N and the uplift of the Qinling Mountains to the S, since the Cenozoic. The fault dips northward (60–80°) and strikes W–E, extending from Qingjiangkou to Xitangyu, Fengyukou, and finally terminates at Daiyu, for a total length of 220 km. The N and S walls of the fault correspond to the loess plateau of the Weihe Basin and to the Qinling Mountains, respectively. Satellite images show clear linear feature for the fault; additionally, Bouguer gravity anomaly and aeromagnetic clearly indicate the occurrence of a density gradient zone along the fault (Peng et al., 1992, 2017). The North Qinling Fault can be divided into three segments according to its geometric characteristics and tectonic landforms. The western segment extends from Qingjiangkou to Xitangyu, is about 73 km long, and its approximate strike direction is SE; the middle segment extends from Xitangyu to Fengyukou, is about 90 km long, and its approximate strike direction is E–W; finally, the eastern segment extends from Fengyukou to Daiyu, is about 47 km long, and its approximate strike direction is E–W; (Zhang et al., 1991, Shaanxi Earthquake; Agency, 1996; Bai, 2018).

Previous research mainly focused on the vertical component of the North Qinling Fault. Under a of normal

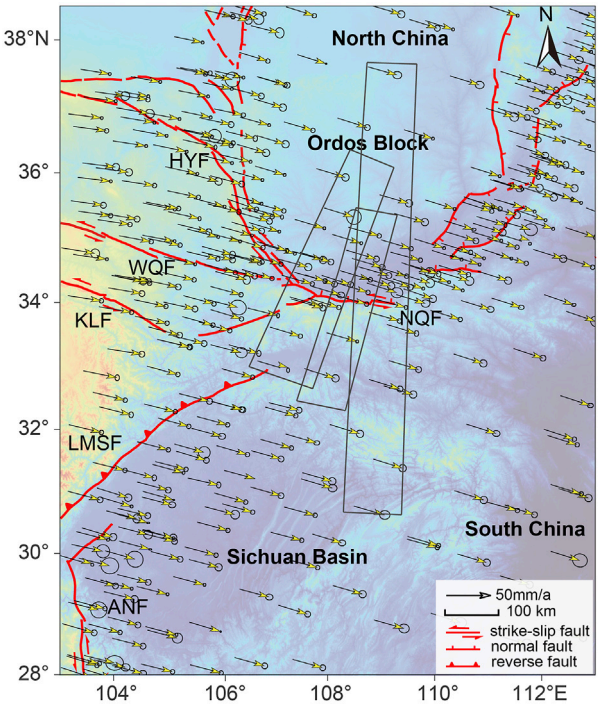

FIGURE 2
Distribution of the GPS velocity profiles across the North Qinling Fault. The black boxes indicate the profiles used for the computation of fault slip rate and locking depth. HYF, Haiyuan Fault; WQF, West Qinling Fault; KLF, Kunlun Fault; LMSF, Longmenshan Fault; ANF, Anninghe Fault; NQF, North Qinling Fault. The fault data were sourced from Zhang et al. (2013).

fault movement, the N wall has been descending, while the S wall has been ascending since the beginning of the Tertiary. Fault scarps of different scales and vertical offsets> 10 km were observed along the fault (Han et al., 2001; Liu et al., 2013; Huang et al., 2020). Regarding present-day fault activity, both the slip rate and the locking depth of the eastern segment are larger than those of the western-middle segments (Cui et al., 2019). Notably, the North Qinling Fault also shows obvious traces of sinistral strike-slip movements, which have horizontally offset rivers and terraces located in front of the Qinling Mountains (Shentu et al., 1991; Peng et al., 1992; Liu et al., 2013.; Ma, 2020).

3 Data and methods

3.1 GPS data

The GPS data used in this study come from Wang and Shen (2020). Our study mainly considered data from campaign and continuous GPS sites included in the Crustal Movement Observation Network of China (CMONOC) I and

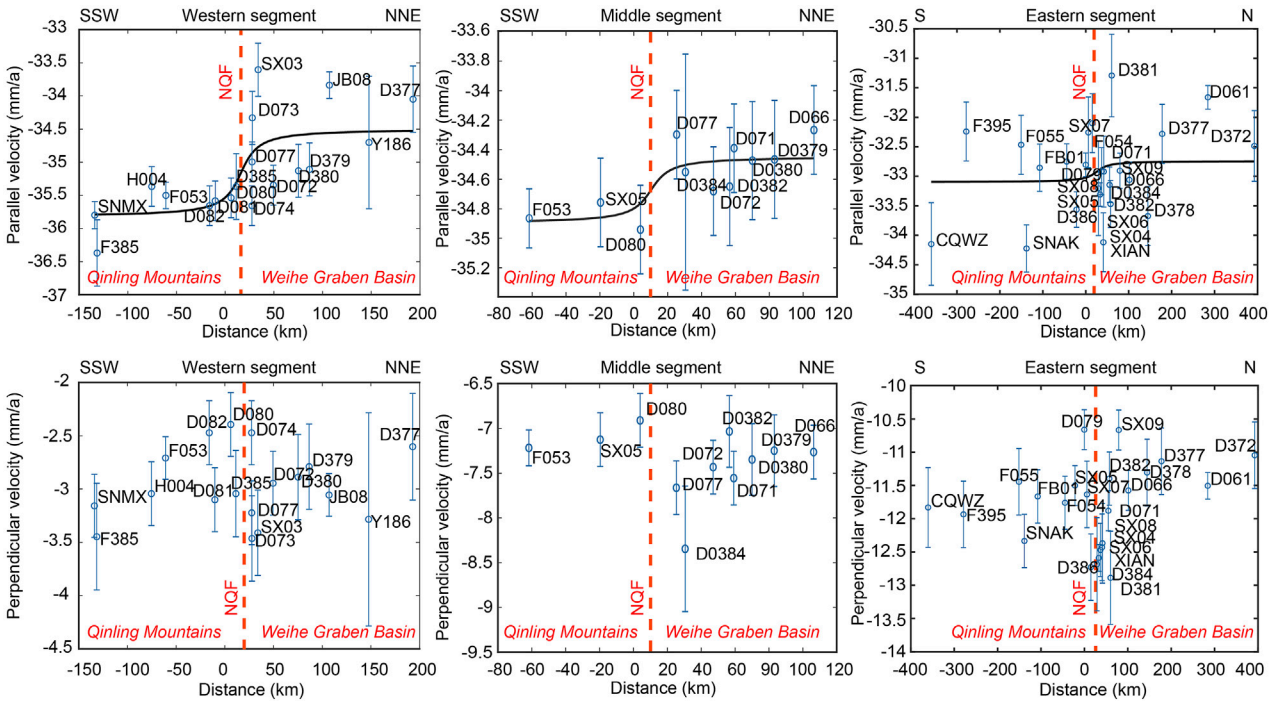

FIGURE 3
GPS velocity profiles. The top graphs refer to the direction parallel to the fault strike, while the bottom graphs refer to the direction perpendicular to the fault strike.

II project. Data from the continuous GPS sites, the campaign GPS sites of CMONOC I, and the continuous GPS sites, the campaign GPS sites of CMONOC II covered the following time spans: 1999–2016 and 1999–2015, 2009–2016 and 2009–2015, respectively. As detailed in Wang and Shen (2020), the raw GPS data obtained from 100 globally distributed IGS sites were processed all together using the GAMIT (Herring et al., 2010) software to ensure solutions of high quality and homogeneity. Particularly, the post-seismic and co-seismic deformation caused by large earthquakes have been modeled using the QOCA software (https://gipsy.jpl.nasa.gov/~qoca). In this study, the co-seismic offsets and effects of the 2005 Sumatra, 2008 Wenchuan, and 2011 Tohoku–Oki earthquakes were considered and corrected. Meanwhile, the stations with low quality (observated by the GeoTracer receiver/antenna during 1999 and 2000) and disturbed by anthropogenic activities (such as ground water and oil pumping, coal mining, etc.,) are discarded.

3.2 Viscoelastic coupling model

GPS velocity field refers to the velocities occurring parallelly and perpendicularly to a fault: they represent the strike-slip rate and the compression rate, respectively, and quantify crust activity. According to the characteristics of the GPS station and our fault segmentation, we selected three velocity profiles along the North Qinling Fault that were orthogonal to the fault strike (Figure 2). The GPS rates were decomposed into fault-parallel and fault-perpendicularly components to obtain the correspondent projection values (Figure 3). Then, the velocity component parallel to the fault strike (i.e., the strike-slip rate of the fault) was inverted. According to the viscoelastic coupling model, considering the locking depth as a dividing line, no slip movement should occur between the surface and the locking depth, but rather below the locking depth. The basic relationship among the locking depth, the long-term slip rate, and the surface movement during the horizontal slipping of the fault was obtained based on the traditional dislocation model (Savage and Burford, 1973; Savage et al., 1999):

$$V_z(x) = b_o - \frac{b_i}{\pi}\arctan\left[\frac{(x - x_i)}{h_i}\right]$$

where $V_z(x)$ is the pre-seismic slip rate of the surface, b_0 the adaptability constant, b_i is the long-term slip rate, x is the fault depth, and h_i is the locking depth at x_i. The thickness of the elastic plastic transition zone in the upper lower crust is determined to be 0 km. The determined slip rates and locking depths are shown in Table 1.

TABLE 1 Comparison between different segments of the North Qinling Fault.

Segment	Length (km)	Strike	Inversion results		90% seismic cutoff focal depth (km)	M_w	Seismic moment (10^{19} N m)	Geological slip rate (mm/a)	References
			Slip rate (mm/a)	Locking depth (km)					
Western	73.57	120°	1.33	13.54	18.4	7.23	8.81	0.29	Zhang et al., (1990) and Bai, (2018)
Middle	90.02	120°	0.45	8.58	16.97	7.35	12.02	0.61	
Eastern	47.01	90°	0.36	21.46	24	7.03	4.42	0.477	

The table shows the fault geometry, slip rate and locking depth (inverted from GPS, data), the 90% seismic cutoff focal depth, M_w, seismic moment, and geologic slip rate at the western, middle, and eastern segments of the North Qinling Fault.

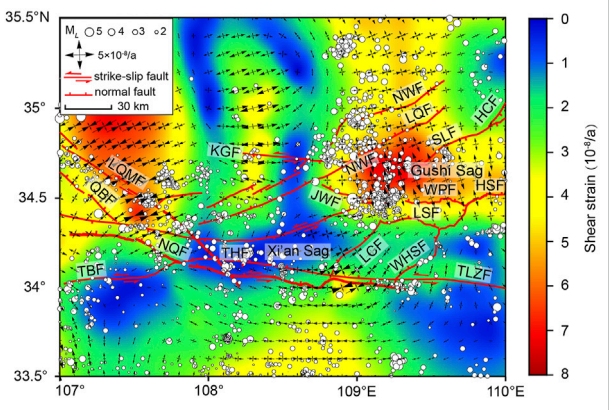

FIGURE 4
Shear strain, principal strain, active fault and modern earthquake distribution in the Weihe Basin (relocated earthquakes from January 1970 to May 2022).

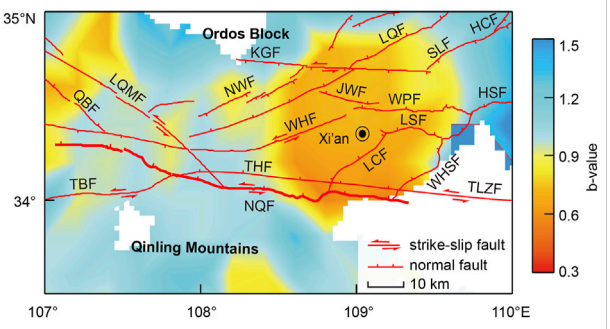

FIGURE 5
Seismic b-values and active fault distribution in the Weihe Basin.

3.3 Strain field calculation

We collected GPS velocity field data published recently (Wang and Shen, 2020) and selected those with errors< 1.5 mm/a. The improved least-square collocation method, which has a good resolution and reliability, was employed here to calculate the regional strain fields (Zhang et al., 1998; Wu et al., 2009; Shen et al., 2015). In the calculation process, it was fundamental to identify the best smoothing factor D, as well as to select a suitable interval distance range (0–500 km) and step length (1 km), in order to meet the following conditions:

$$W = \sum_{n=1}^{\#_{sta}*2} Z(i)*L(i) \gg W_t$$

where L is the weight of the distance correlation and Z is the weight of the spatial site distribution. In the calculation process, the data points over the threshold L_{max} = 10 × D km (from the calculation point) are excluded, and the optimal smoothing factor D is obtained under the condition of satisfying W_t, as well as the velocity and strain tensors [U_x, U_y, τ_x, τ_{xy}, τ_y, ω] T of all the GPS stations. In case of a sparse station distribution, the selection function $L(i) = 1/(1+\Delta Ri2/D2)$ is used instead, where ΔR is the distance between the station and the interpolation point. Station distribution and distance weighting were both considered to ensure the reliability and accuracy of the strain fields (see Figure 4).

3.4 Seismic b-value calculation

Data on modern earthquakes (that occurred between January 1970 and May 2022) were obtained from the China Earthquake Networks Center. The time series change of the minimum magnitude of completeness (Mc) in the Weihe Basin was qualitatively analyzed according to the magnitude-order method (Ogata et al., 1991) and the entire magnitude range (EMR) method (Woessner and Wiemer, 2005). The earthquake catalog of the Weihe Basin was analyzed starting from 1970, and Mc was determined considering it equal to M_L2.0. Earthquakes ≥ Mc were selected and the least square method was used to

calculate the b-values. Gridding was performed considering an interval of 0.2°, and earthquakes in the circular statistical unit with a radius of 30 km were selected. The number of events in each grid node had to be ≥ 20 in order to be considered for the calculations. For statistical grid nodes that could not meet the criteria, the statistical radius was increased to 50 km. If, after this, the number of samples was still < 20, the b-values were not calculated. The b-values are shown in Figure 5.

4 Results

4.1 Locking depths and slip rates

The distribution of GPS velocity field shows that the movement direction of the Weihe Basin is roughly SE–E. Additionally, the GPS velocity component profile fitting curve parallel to the fault is characterized by sinistral shear strain accumulation, while there is no obvious transverse compression deformation (Figure 3). The accumulation of horizontal shear strain varies along different segments, and the accumulated shear strain decreases from W to E. Detailed features were identified for each segment. 1) The GPS velocities obtained for the western segment of the fault (Qingjiangkou–Xitangyu), parallel to the fault strike, suggest an obvious sinistral strike-slip movement. The inversion results indicate a sinistral strike-slip velocity of 1.33 mm/a and a locking depth of 13.54 km. 2) The GPS velocities obtained for the middle segment of the fault (Xitangyu–Fengyukou), parallel to the fault strike, indicate an obvious sinistral strike-slip movement. The correspondent inversion results indicate a sinistral strike-slip velocity of 0.45 mm/a and a locking depth of 8.58 km. 3) The GPS velocities obtained for the eastern segment of the fault (Fengyukou–Daiyu), parallel to the fault strike, indicate an inapparent sinistral strike-slip movement. The correspondent inversion results indicate a sinistral strike-slip velocity of 0.36 mm/a and a locking depth of 21.46 km. 4) The GPS data obtained for the direction vertical to the fault strike indicate the absence of obvious tensions along the three segments.

4.2 Strain fields

Our GPS inversions showed that, in the Weihe Basin, strains have been controlled by the fault distribution, and been induced by the main fault activity; moreover, they are related to modern seismicity distribution (Figure 4).

4.2.1 Shear and principal strains in the Weihe Basin

The shear strain rate is overall higher in the eastern region and lower in the western region. A low-value area ($< 1 \times 10^{-8}$/a) was identified in the Xi'an Sag, in the southern-central part of the Weihe Basin: it is bounded by the North Qinling Fault to the S, the Lintong–Chang'an Fault to the E, and the Weihe Fault to the N. A median-value area ($\pm 2 \times 10^{-8}$/a) was instead identified in correspondence of the Lishan uplift: it is bounded by the North Qinling Fault to the S, the Lintong–Chang'an Fault to the W, and the Lishan Piedmont Fault to the N. Finally, a high-value area ($> 4 \times 10^{-8}$/a) was found in the Gushi Sag, in the northeastern part of the basin, where many modern small earthquakes have occurred. This corresponds to the intersection area of the Weihe Fault with the Kouzhen–Guanshan Fault, the North Weihe Fault, and the Weinan Plateau Fault. Changes in the principal strain rate and in the direction are regulated by active faults in the Weihe Basin. The western margin of the basin is mainly controlled by the Longxian–Qishan–Mazhao Fault; here, the approximate direction of the principal compressive strain is NE–E. The southern margin of the basin is instead mainly controlled by the North Qinling Fault, which induces a principal compressive strain in the W–E direction. Meanwhile, the western–middle segment of the North Qinling Fault is subjected to the W–E principal compressive strain (consistent with the fault strike direction). The eastern segment of the fault is instead affected by a fault zone characterized with a N–NE strike (which includes the Lintong–Chang'an Fault and the West Huashan Fault), and the direction of the principal compressive strain is also N–NE. In the northeastern part of the North Weihe Fault, the main compressive strain occur in the NE–E direction. Meanwhile, in the Gushi Sag, it occurs in the N–NW direction, and its high principal strain rate corresponds to the region characterized by a high concentration of modern earthquakes.

4.2.2 Shear and principal strains along the North Qinling Fault

The shear strain rate shows an obvious gradient at the intersection of the Weihe Basin with the Qinling Mountains, controlled by the North Qinling Fault. Along this fault, the shear strain rate in the N wall is lower than that in the S wall; moreover, the shear strain rate changes considerably along the fault strike. The shear strain rate values in the western-middle segments are lower than that in the eastern segment and quite constant. A high value was noted at the intersection of the eastern segment of North Qinling Fault with the Lintong-Chang'an Fault: here, the maximum observed shear strain rate is 4×10^{-8}/a. The principal strain direction in the southern part of the basin is controlled by the North Qinling Fault and by the N–NE fault zone located to the E of it. The principal strain rate gradually increases from W to E along the North Qinling Fault, reaching its maximum value at the intersection of the North Qinling Fault with the Lintong–Chang'an Fault, where modern small earthquakes have not are rather weak.

4.3 Seismic b-values

The b-value distribution in the Weihe Basin is clearly shown in Figure 5. Higher and lower b-values occur in the

eastern and western parts of the Weihe Basin, respectively. Along the North Qinling Fault, the b-values also differ significantly from W to E, and the eastern part has the lowest b-values in the Weihe Basin. The average b-values for the eastern segment of the North Qinling Fault and Weihe Basin (0.6 ± 0.1 and 0.8 ± 0.1, respectively) are both lower than the average b-values for the western–middle segment of the North Qinling Fault (1.0 ± 0.1) over the same period.

5 Discussion

5.1 Stability analysis

5.1.1 Locking depths

Cui et al. (2019) proposed locking depths of 7.7 ± 3.58 km and 10 ± 4.47 km for the study region, which are different from those determined in this study (13.54 km, 8.58 km, and 21.46 km). Most of the difference might be explained as follows. First, it is important to note that different data sources were used in Cui et al. (2019) and in this study: those authors utilized multi-stage precise leveling data across the North Qinling Fault, while we calculated the locking depths based on GPS horizontal velocities. The influence of large earthquakes on fault movement by the leveling data was not deducted. Meanwhile, during the processing of GPS data, the co-seismic deformation caused by large earthquakes was considered, and troublesome epochs derived from the horizontal velocities were corrected. In this case, the GPS velocity could in fact reflect the crustal deformation by fault movements. Second, the locking depths inversed by considering different fault movements in Cui et al. (2019) and in this study: the leveling data and the GPS data were influenced by the normal faulting and strike-slip movement, respectively. In Shi et al. (2020), inversion of GPS data was applied to investigate a back-arc fault in the Central Andes. In that instance it was demonstrated that, even when data and processing methods are consistent, the calculated locking depths of horizontal and vertical movements can be different. In addition, the ranges and source locations of data used in Cui et al. (2019) and in our study were different. Cui et al. (2019) used two leveling lines that crossed the fault at the intersection of its western and middle segments, as well as the intersection of its middle and eastern segments. While, we selected GPS sites distributed along the whole fault, selecting three profiles according to fault segmentation. In summary, though a variety of factors may influence the correlation between the locking depths from these two methods, the locking depths inverted from the horizontal (i.e., GPS data) and vertical (i.e., leveling data) movements are generally consistent: a greater locking depth is determined for the eastern section of the fault.

5.1.2 GPS and geological slip rates

GPS and geological slip rates provide information on the fault vertical and horizontal movements, respectively (Table 1). Therefore, it is difficult to directly compare the slip rates of different motion types by GPS inversion and geological methods. Besides, geological and GPS slip rates are constrained by different influential factors. GPS measurement involves transient (i.e., generally elastic and some viscous) and permanent (i.e., plastic) components in the present day, whereas geological records only include permanent strain (Meade and Hager, 2005) and depend on the reliability of offset measurements and geochronological data (Cowgill, 2007). Thus, the GPS slip rates tends to differ from geological slip rates along the North Qinling Fault. Below, we discuss fault GPS and geological slip rates separately.

The inversion of GPS data indicates that the slip rate is equal to the velocity below the locking depth currently, and that the slip rate decrease eastwards (Table 1). Notably, the slip rate of the West Qinling Fault is 2.5 ± 0.3 mm/a (Li et al., 2021): larger than that of the North Qinling Fault. This is consistent with the current dynamic background, in which the uplift of the Tibetan Plateau is causing a large-scale sinistral strike-slip movement. The North Qinling Fault, characterized by lower slip rates, is located at the end of the eastward spreading zone. The higher slip rate of the western segment might indicate that this segment is still in a post-seismic stage and is not locked at present. Overall, the GPS and geological slip rates are in the same order of magnitude, supporting and confirming the reliability of methods applied in this study. For the geological evidence, instead, provides information on the strength of single tectonic events in relation to fault activity, and suggests that the slip rate in the western segment is lower than in the middle-eastern segments (Table 1): fault activity and earthquake seismicity should be weaker in the western segment.

5.1.3 Prominence of the North Qinling Fault

The North Qinling Fault is a major structure in a boundary zone characterized by active tectonic blocks (i.e., the North China Block and the South China Block) in mainland China (Figure 2, Zhang et al., 2013), and separates the Weihe Basin from the Qinling Mountains. We collected evidence that the North Qinling Fault is the most active and largest structure in the Weihe Basin, and it subjects the area to a high earthquake hazard. The crust structure determined based on the receiving function and deep seismic reflection, clearly indicates that the North Qinling Fault cuts off the Moho, reaching a depth of about 40 km, while the other faults occurring in the basin cut off only the upper crust (Xu et al., 2014; Guo and Chen, 2016; Si et al., 2016; Li et al., 2017; Shen et al., 2022; Zhang et al., 2022). Besides, the results of a geological survey suggest these other faults, characterized by lower geological slip rates and activities, are capable of generating only moderate earthquakes, differently from the North Qinling Fault (Shaanxi Earthquake Agency,

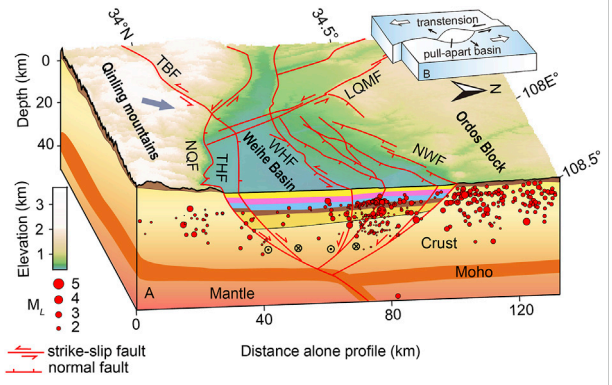

FIGURE 6
A Structural model of the Weihe Basin. B Model of the pull-apart basin.

1996). According to the above information, we can infer that the North Qinling Fault has a much higher activity and seismic potential than nearby (shallower cutting) faults. Therefore, our inversion results should mainly reflect the slip rates and locking depths of the North Qinling Fault.

5.2 Strike-slip movement of the North Qinling Fault

Some scholars argued that, since the Late Miocene–Quaternary, normal faulting has been predominant in the North Qinling Fault, which bounds the southern part of the Weihe Basin and controls its subsidence and sedimentation (Wang, 1965; Liu et al., 1981; Wang, 1986; Xie et al., 1991; Zhang et al., 1991; Li, 1992; Peng et al., 1992; Shaanxi Earthquake Agency, 1996; Han et al., 2001; Xie, 2011; Ren et al., 2012, 2013; Rao et al., 2014; Meng, 2017). Still, other studies suggest that the North Qinling Fault is currently characterized by a large-scale sinistral strike-slip movement, due to a NW–SE tensile stress affecting the Weihe Basin and caused by the eastward spreading of the Tibetan Plateau (Molnar and Tapponnier, 1975; Peltzer et al., 1985; Tapponnier et al., 1986; Zhang et al., 1995; Zhang et al., 1998; Zhang et al., 1999; Zhang et al., 2005; Zhang et al., 2019; Sun, 2005; Zhang et al., 2006; Sun and Xu, 2007; Liu et al., 2013).

In this study, the inversion of principal strain obtained from GPS data (Figure 4) indicate that strike-slip has been the primary movement mode of the North Qinling Fault for decades. Below, we discuss information suggesting that the North Qingling Fault is a sinistral strike-slip fault, whose shearing and tension control the formation of a pull-apart basin (i.e., the Weihe Basin) (Figure 6).

1) Geological survey has provided evidence of recent horizontal offset along most active faults in the Weihe Basin, and especially along the North Qinling Fault (Shentu et al., 1991; Peng et al., 1992; Liu et al., 2013.; Bai, 2018; Ma, 2020; Ma, 2020). 2) Prospecting and artificial seismic exploration have demonstrated that the crust in correspondence of the Weihe Basin is characterized by a large-scale "negative flower structure" (Zhang et al., 2021), resulting from shearing and tension. 3) Cenozoic sediments have a large thickness (> 7500 m) in the Weihe Basin, and the Quaternary sedimentary rate is high (465 m/Ma) (Sun and Xu, 2007). These are characteristics correspond to those typical of pull-apart basins. 4) The GPS velocity field suggests NW-SE movements in the Weihe Basin (England and Houseman, 1989; Clark and Royden, 2000; Qu et al., 2016), moreover, the stress field constrained by seismic activity and focal mechanism solutions indicates that the maximum horizontal principal stress direction is nearly EW along the North Qinling Fault (Yu et al., 2022), which is consistent with our studies.

5.3 Seismicity along the North Qinling Fault

5.3.1 Modern seismicity

To analyze modern seismicity along the North Qinling Fault, we selected relocated earthquakes from the period January 1970–May 2022 with the epicenter within 20 km from the reference profile following the direction of the fault strike, and drew the seismic depth transect along the North Qinling Fault (Figure 7). Although earthquakes involved in the transect refer to other faults, such as the Taochuan–Huxian Fault, the Lintong–Chang'an Fault and other secondary faults. Among them, the Taochuan–Huxian Fault can be regarded as a branch of the North Qinling Fault. Moreover, there is no explicit evidence that the Lintong–Chang'an Fault is a Holocene active fault. Hence, our seismic profile basically reflects the current seismicity along the North Qinling Fault.

The focal depth of the North Qinling Fault is generally within 30 km, but it is unevenly distributed along the fault. Notably, modern earthquakes have occurred mainly along the western and middle segments of the fault. In particular, a relatively high concentration of earthquakes was identified in the shallow layer (0–3 km) of the western and middle segments, while a clear seismic gap was revealed in the eastern segment. These facts highlight a sharp contrast in the seismicity of the western-middle and eastern segments.

5.3.2 Paleoearthquake

Although historical and modern earthquakes and rather weak along the North Qinling Fault, there is sufficient evidence of paleoearthquakes, prehistoric landslides, and barrier lakes caused by strong earthquakes along the fault (Bai, 2018; Huang et al., 2020; Yang, 2022). Paleoearthquake information can make up for deficiencies in historical and

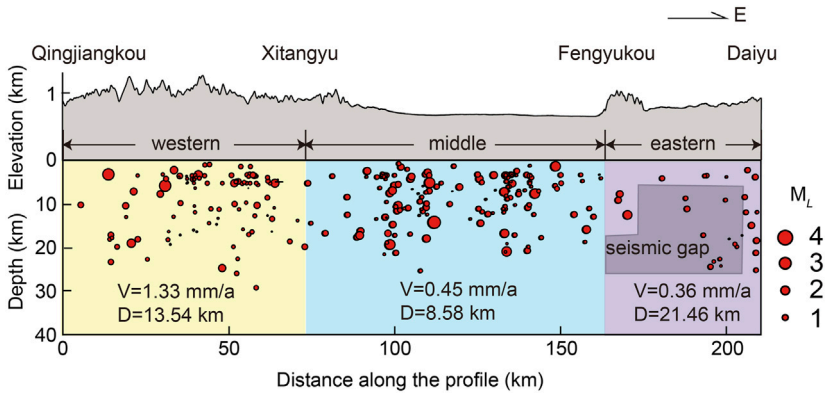

FIGURE 7
Elevation and seismic depth along the North Qinling Fault. A seismic gap can be identified in the area with sparse earthquakes.

modern seismicity information and can be used to explore the occurrence regularity of strong earthquakes along active faults over long time scales (McCalpin, 1996; Caputo and Helly, 2008). Previous studies have shown that, along the North Qinling Fault, the average recurrence interval of prehistorical earthquakes is about 3,000 years (Zhang et al., 1990; Shaanxi Earthquake Agency, 1996; Bai, 2018). By combining this information with the occurrence time of the last major earthquake, we can infer that the fault is now in a pre-seismic stage: it is approaching the recurrence period of large earthquakes.

5.4 Seismic potential of the North Qinling Fault

5.4.1 Segmentation characteristics

In this study, we adopted a segmentation that reflects the geometry of the fault, as determined from the geological survey (Zhang et al., 1991; Shaanxi Earthquake Agency, 1996; Bai, 2018). Inversions of GPS data and b-values were used to define the diversity between segments. The eastern segment, having the deepest locking depth, the highest shear and principal strain rates, the lowest b-values, and presenting a seismic gap, is the most unique. These differences suggest that, even under a homogeneous tectonic background, different segments would experience discrepant geological and present-day activities. This justifies our choice of the segmentation method, which is able to provide detailed spatial information on fault activity. On this basis, we conducted a comprehensive analysis of the fault seismic potential and timing.

5.4.2 b-values and strain fields

The b-value is typically inversely related with effective stress and closely related to the fault asperity. Large earthquakes usually occur in areas characterized by low b-values, and where a higher amount of stress is accumulated (Wiemer and Wyss, 1997; Wyss et al., 2004; Yi et al., 2006; Zhu and Huang., 2022). Thus, we employed the seismic b-value as an indicator of accumulated stress to further discuss the seismic potential of the fault. The lower average b-values of the eastern segment (Figure 5), compared to those of the other segments, indicates that a higher amount of stress is accumulated here and hence, that this area has a higher seismic potential.

The shear and principal strains typically reflect the current stress state of the crust. We noted that the shear strain and principal strain rates are both higher in the eastern segment than in the western-middle segments of the North Qinling Fault: the highest strain rates are registered at the intersection of the North Qinling Fault with the Lintong–Chang'an Fault. However, unlike the Gushi Sag (in the northeastern part of the basin), the eastern segment of the North Qinling Fault is not a seismically active area (Figure 4). Overall, the high strain rates (Figure 4) and low average b-values (Figure 5) of the eastern segment, as well as the occurrence of a seismic gap (Figure 7), indicate that a large amount energy should have accumulated in this area.

5.4.3 Moment magnitude and focal depth-frequency

Extensive research has been conducted on the relationship between earthquake moment magnitude and surface rupture length (Tocher, 1958; Slemmos, 1977; Long et al., 2006; Ran et al., 2011). In this paper, according to the empirical relationship between moment magnitude (M_W) and rupture length (L) in global strike-slip faults ($M_W = 5.16 + 1.12$ L gL, where L is in km) (Wells and Coppersmith, 1994), as well as the empirical relationship $M_W = 2/3$ (lgMo−16.1) (Chen and Liu, 2018), we calculated the moment magnitude and the seismic moment of the western, middle, and eastern segments of the North Qinling Fault. Our statistical results (Table 1) indicate that this fault has the capability of generating earthquakes with $M_W > 7$.

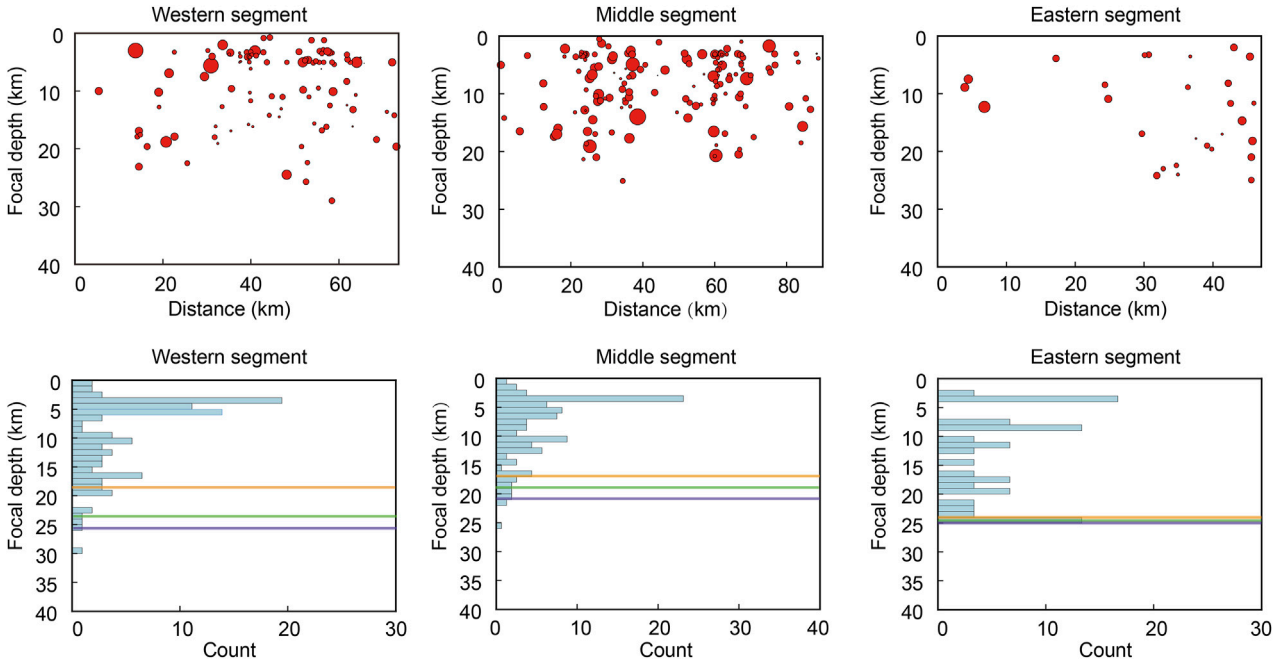

FIGURE 8
Focal depth distribution along the North Qinling Fault. The orange, green, and purple lines represent the 90%, 95%, and 99% seismic cutoff depths, respectively.

Our calculation demonstrates a strong earthquake capacity for the North Qinling Fault. The western-middle segments have shallower locking depths (i.e., 13.54 km and 8.58 km, respectively) than the eastern segment (i.e., 21.46 km) and present earthquake clustering, implying energy release. This information, combined with other results obtained in this study, implies that the eastern segment may be locked. Below, this issue is discussed quantitatively by considering the focal depth.

Previous research has demonstrated a good correspondence between the 90% seismic cutoff focal depth and the locking depth (Miller and Furlong, 1988; Williams, 1996; Richards and Shearer, 2000; Bonner et al., 2003). A comparative analysis of these depths can thus help clarifying the seismic potential of a fault. When the locking depth is shallower than the 90% seismic cutoff focal depth, "deep creep" occurs between the locking depth and the focal depth layers; in this case, stress mainly accumulates above the locking depth and major earthquakes are unlikely. When the locking depth is close to the 90% seismic cutoff depth, however, the fault is locked (Wdowinski, 2009; Schmittbuhl et al., 2015). Here, we discuss the seismic potential of the Qinling Fault by comparing the 90% seismic cutoff focal depth (within a width of 20 km and for different segments) with the locking depth (Figure 8; Table 1). The result indicates that the locking depth of the western segment should be 13.54 km [shallower than the 90% seismic cutoff depth (18.4 km)], suggesting the occurrence of "deep creep" in the layer between 13.45 and 18.4 km. The locking depth of the middle segment should be 8.58 km [only half of the 90% seismic cutoff depth (16.97 km)], suggesting the occurrence of "deep creep" in the layer between 8.58 and 16.97 km. Finally, the locking depth of this eastern segment should be 21.46 km [similar to the 90% seismic cutoff depth (24 km)], indicating that this segment is locked.

Overall, the results of our analyses suggest that the North Qinling Fault is presently in a pre-seismic stage and exhibits significant segmentation characteristics: the eastern segment, characterized by higher strain rates and accumulated stress, is obviously locked and capable of generating strong earthquakes in the near future.

6 Conclusion

Based on GPS data and seismic activity, we inverted slip rate, locking depth, shear and principal strain fields to determine the present-day activity and seismic potential of the North Qinling Fault. Our main findings are summarized below.

The North Qinling Fault, characterized by a sinistral strike-slip movement, is currently in a pre-seismic stage and makes the Weihe Basin an area of high earthquake hazard. This fault can in fact potentially generate $M_W > 7$ earthquakes. Its eastern segment, where the locking depth is close to the 90% seismic

cutoff focal depth, has relatively higher shear and principal strain rates, low b-values, and presents a seismic gap. These traits collectively suggest that the eastern segment is currently locked, and that it has a strong seismic potential that might be expressed in the near future. Therefore, a continuous, careful monitoring of this area is required.

Data availability statement

The original contributions presented in the study are included in the article/Supplementary Material, further inquiries can be directed to the corresponding author.

Author contributions

CY: Conceptualization, formal analysis, funding acquisition, methodology, software, visualization, writing—original draft. LJ: Formal analysis, methodology, writing—review and editing. YY: Conceptualization, writing—review and editing, funding acquisition. LS: Conceptualization, software. YW: Software. HS: Conceptualization.

Funding

This work was jointly supported by the Natural Science Basic Research Program of Shaanxi Province (Grant No. 2022JQ-298), the National Natural Science Foundation of China (Grant No. 42004048), and the Seismological Research Tracking Project of China Earthquake Administration (Grant No. 2022010212). Most figures were generated by using the Generic Mapping Tools software (Wessel and Smith, 1995). The relocated earthquake catalogue was provided by Liu C. and Zhang E. H.

Acknowledgments

The authors are grateful to Shi F. Q. for helpful discussion, and to Zhang W. T. and Chen X. X. for software assistance.

Conflict of interest

The authors declare that the research was conducted in the absence of any commercial or financial relationships that could be construed as a potential conflict of interest.

Publisher's note

References

Bai, X. D. (2018). *Influence study from the activity of the northern margin fault zone of Qinling Mountains on geological hazard*. Beijing, China: Institute of Engineering Mechanics, China Earthquake Administration.

Becker, T. W., Hardebeck, J. L., and Anderson, G. (2005). Constraints on fault slip rates of the southern California plate boundary from GPS velocity and stress inversions. *Geophys. J. Int.* 160 (2), 634–650. doi:10.1111/j.1365-246X.2004.02528.x

Bonner, J. L., Blackwell, D. D., and Herrin, E. T. (2003). Thermal constraints on earthquake depths in California. *Bull. Seismol. Soc. Am.* 93 (6), 2333–2354. doi:10.1785/0120030041

Caputo, R., and Helly, B. (2008). The use of distinct disciplines to investigate past earthquakes. *Tectonophysics* 453 (1-4), 7–19. doi:10.1016/j.tecto.2007.05.007

Chen, Y. G., Ding, K. H., Wang, Q., He, P., Li, S. P., and Qiao, X. J. (2020). A refined slip distribution of the 2013 M w 6.7 Lushan, China earthquake constrained by GPS and levelling data. *Geophys. J. Int.* 222 (1), 572–581. doi:10.1093/gji/ggaa202

Chen, Y. T., and Liu, R. F. (2018). Moment magnitude and its calculation. *Earthq. Res. China* 39 (2), 1–9. doi:10.3969/j.issn.1003-3246.2018.02.001

Clark, M. K., and Royden, L. H. (2000). Topographic ooze: Building the eastern margin of Tibet by lower crustal flow. *Geology* 28 (8), 703–706. doi:10.1130/0091-7613(2000)028<0703:tobtem>2.3.co;2

Cowgill, E. (2007). Impact of riser reconstructions on estimation of secular variation in rates of strike–slip faulting: Revisiting the Cherchen River site along the Altyn Tagh Fault, NW China. *Earth Planet. Sci. Lett.* 254 (3-4), 239–255. doi:10.1016/j.epsl.2006.09.015

Cui, D. X., Hao, M., Qin, S. L., and Wang, W. P. (2019). Inversion of fault dip-slip rate and locking depth in Central-Southern Shaanxi of China. *Chin. J. Geophys.* 62 (12), 4648–4657. doi:10.6038/cjg2019M0358

Deng, Q. D., Zhang, P. Z., Ran, Y. K., Yang, X. P., Min, W., and Chu, Q. Z. (2002). Basic characteristics of active tectonics in China. *Sci. China (D)* 32 (12), 1020–1030. doi:10.3321/j.issn:1006-9267.2002.12.007

Deng, Q. D., Zhang, P. Z., Ran, Y. K., Yang, X. P., Min, W., and Chen, L. C. (2003). Active tectonics and earthquake activities in China. *Earth Sci. Front.* 10 (8), 66–73. doi:10.3321/j.issn:1005-2321.2003.z1.012

Du, F., Wen, X. Z., Feng, J. G., Liang, M. J., Long, F., and Wu, J. (2018). Seismotectonics and seismic potential of the Liupanshan fault zone (LPSFZ), China. *Chin. J. Geophys.* 61 (2), 545–559. doi:10.6038/cjg2018L0181

Du, F., Wen, X. Z., and Zhang, P. Z. (2010). Post-seismic slip and deformation on the Luhuo segment of the Xianshuihe fault zone. *Chin. J. Geophys.* 53 (10), 2355–2366. doi:10.3969/j.issn.0001-5733.2010.10.009

Du, F., Wen, X. Z., Zhang, P. Z., and Wang, Q. L. (2009). Interseismic deformation across the Longmenshan fault zone before the 2008 M8. 0 Wenchuan earthquake. *Chin. J. Geophys.* 52 (11), 2729–2738. doi:10.3969/j.issn.0001-5733.2009.11.007

England, P. C., and Houseman, G. A. (1989). Extension during continental convergence, with application to the Tibetan Plateau. *J. Geophys. Res.* 94 (17), 17561–17597. doi:10.1029/JB094iB12p17561

Fialko, Y. (2006). Interseismic strain accumulation and the earthquake potential on the southern San Andreas fault system. *Nature* 441 (7096), 968–971. doi:10.1038/nature04797

Guo, Z., and Chen, Y. J. (2016). Crustal structure of the eastern Qinling orogenic belt and implication for reactivation since the Cretaceous. *Tectonophysics* 683, 1–11. doi:10.1016/j.tecto.2016.06.007

Han, H. Y., Mi, F. S., and Liu, H. Y. (2001). Geomorphological structure in the Weihe Basin and neotectonic movement. *J. Seismol. Res.* 24 (3), 251–257. doi:10.3969/j.issn.1000-0666.2001.03.011

Herring, T. A., King, R. W., and McClusky, S. C. (2010). *GAMIT reference manual, GPS Analysis at MIT, Release 10.4*. Cambridge, MA: Massachusetts Institute of Technology.

Huang, W. L., Yang, Q. H., Yan, L., Su, S. R., and Zhou, Z. H. (2020). Relationship between distribution characteristics of prehistoric landslides and seismic activity along qinling piedmont fault. *J. Eng. Geol.* 28 (6), 1259–1271. doi:10.13544/j.cnki.jeg.2019-383

Huang, Y., Qiao, X. J., Freymueller, J. T., Wang, Q., Yang, S. M., Tan, K., et al. (2019). Fault geometry and slip distribution of the 2013 Mw 6.6 Lushan earthquake in China constrained by GPS, InSAR, leveling, and strong motion data. *J. Geophys. Res. Solid Earth* 124 (7), 7341–7353. doi:10.1029/2019JB017451

Li, H. Q., Gao, R., Xiong, X. S., Wang, H. Y., and Li, W. H. (2017). Moho fabrics of North Qinling belt, Weihe graben and Ordos block in China constrained from large dynamite shots. *Geophys. J. Int.* 209 (2), 643–653. doi:10.1093/gji/ggx052

Li, J. Y., Zhou, B. G., Li, T. M., Yang, Y. L., Li, Z. F., and Long, F. (2020). Seismogenic depths of the Anninghe-Zemuhe and Daliangshan fault zones and their seismic hazards. *Chin. J. Geophys.* 63 (10), 3669–3682. doi:10.6038/cjg2020N0201

Li, X., Pierce, I. K. D., Bormann, J. M., Hammond, W. C., Zhang, Z., Li, C., et al. (2021). Tectonic deformation of the northeastern Tibetan Plateau and its surroundings revealed with GPS block modeling. *JGR. Solid Earth* 126 (5), e2020JB020733. doi:10.1029/2020JB020733

Li, Y. S. (1992). *Research on ground fissure in Xi'an region and active faults in Weihe basin*. Beijing, China: Seismological Press.

Liu, J. H., Zhang, P. Z., Lease, R. O., Zheng, D. W., Wan, J. L., Wang, W. T., et al. (2013). Eocene onset and late Miocene acceleration of Cenozoic intracontinental extension in the North Qinling range–Weihe graben: Insights from apatite fission track thermochronology. *Tectonophysics* 584, 281–296. doi:10.1016/j.tecto.2012.01.025

Liu, Q., Wen, X. Z., and Shao, Z. G. (2016). Joint inversion for coseismic slip of the 2013 Ms7. 0 Lushan earthquake from GPS, leveling and strong motion observations. *Chin. J. Geophys.* 59 (6), 2113–2125. doi:10.6038/cjg20160617

Liu, S. W., and Gan, J. S. (1981). The Fenwei rift valley system. *Crustal Deform. Earthq.* 3, 110–123.

Long, F., Wen, X. Z., and Xu, X. W. (2006). Empirical relationships between magnitude and rupture length, and rupture area, for seismogenic active faults in north China. *Seismol. Geol.* 28 (4), 511–535. doi:10.3969/j.issn.0253-4967.2006.04.001

Ma, J. (2020).*1556 Hua County M8 Surface rupture and seismogenic structure of magnitude earthquake*. Doctoral dissertation. Beijing, China: Institute of Geology, China Earthquake Administration.

McCalpin, J. (1996). *Paleoseismology*. San Diego: Academic Press.

Meade, B. J., and Hager, B. H. (2005). Block models of crustal motion in southern California constrained by GPS measurements. *J. Geophys. Res.* 110 (B3), B03403–B03419. doi:10.1029/2004JB003209

Meng, Q. R. (2017). Origin of the qinling Mountains. *Sci. Sin. Terrae* 47 (4), 412–420. doi:10.1360/N072016-00422

Miller, C. K., and Furlong, K. P. (1988). Thermal-mechanical controls on seismicity depth distributions in the San Andreas Fault Zone. *Geophys. Res. Lett.* 15 (12), 1429–1432. doi:10.1029/GL015i012p01429

Molnar, P., and Tapponnier, P. (1975). Cenozoic Tectonics of Asia: Effects of a Continental Collision: Features of recent continental tectonics in Asia can be interpreted as results of the India-Eurasia collision. *Science* 189 (4201), 419–426. doi:10.1126/science.189.4201.419

Ogata, Y., Imoto, M., and Katsura, K. (1991). 3-D spatial variation of b-values of magnitude-frequency distribution beneath the Kanto District, Japan. *Geophys. J. Int.* 104 (1), 135–146. doi:10.1111/j.1365-246X.1991.tb02499.x

Papanikolaou, I. D., Roberts, G. P., and Michetti, A. M. (2005). Fault scarps and deformation rates in Lazio–Abruzzo, Central Italy: Comparison between geological fault slip-rate and GPS data. *Tectonophysics* 408 (1-4), 147–176. doi:10.1016/j.tecto.2005.05.043

Parsons, T. (2006). Tectonic stressing in California modeled from GPS observations. *J. Geophys. Res.* 111 (B3), B03407. doi:10.1029/2005JB003946

Peltzer, G., Tapponnier, P., Zhang, Z. T., and Qin, X. Z. (1985). Neogene and quaternary faulting in and along the qinling Shan. *Nature* 317 (6037), 500–505. doi:10.1038/317500a0

Peng, J. B., Lu, Q. Z., and Huang, Q. B. (2017). *Earth fissures of fenwei basin*. Beijing, China: Science Press.

Peng, J. B., Zhang, J., and Su, S. R. (1992). *Active faults and geological hazards in Weihe basin*. Xi'an, China.

Perez, O. J., and Jacob, K. H. (1980). Tectonic model and seismic potential of the eastern Gulf of Alaska and Yakataga seismic gap. *J. Geophys. Res.* 85 (B12), 7132–7150. doi:10.1029/JB085iB12p07132

Qu, W., Wang, Y. S., Zhang, Q., Wang, Q. L., and Xue, K. (2016). Current crustal deformation variation characteristics of the Fenwei basin and its surrounding areas revealed by GPS data. *Chin. J. Geophys.* 59 (3), 828–839. doi:10.6038/cjg20160306

Ran, H. L. (2011). Empirical relations between magnitude and parameters of strike-slip seismogenic active faults associated with historical earthquakes in Western China. *Seismol. Geol.* 33 (3), 577–585. doi:10.3969/j.issn.0253-4967.2011.03.008

Rao, G., Lin, A. M., Yan, B., Jia, D., and Wu, X. J. (2014). Tectonic activity and structural features of active intracontinental normal faults in the Weihe Graben, central China. *Tectonophysics* 636, 270–285. doi:10.1016/j.tecto.2014.08.019

Ren, J., Feng, X., Wang, F., Peng, J., Liu, C., Dai, W., et al. (2013). Fine crust structures of Xi'an sag in the Weihe basin revealed by a deep seismic reflection profile. *Chin. J. Geophys.* 56 (2), 513–521. doi:10.6038/cjg20130215

Ren, J. (2012). *Probe on the deep crustal structure in Weihe Basin and tectonics research of basin*. Xi'an, China: Chang'an University.

Richards-Dinger, K. B., and Shearer, P. M. (2000). Earthquake locations in southern California obtained using source-specific station terms. *J. Geophys. Res.* 105 (B5), 10939–10960. doi:10.1029/2000JB900014

Savage, J. C., and Burford, R. O. (1973). Geodetic determination of relative plate motion in central California. *J. Geophys. Res.* 78 (5), 832–845. doi:10.1029/JB078i005p00832

Savage, J. C., Svarc, J. L., and Prescott, W. H. (1999). Geodetic estimates of fault slip rates in the San Francisco Bay area. *J. Geophys. Res.* 104 (B3), 4995–5002. doi:10.1029/1998JB900108

Schmittbuhl, J., Karabulut, H., Lengliné, O., and Bouchon, M. (2015). Seismicity distribution and locking depth along the main marmara fault, Turkey. *Geochem. Geophys. Geosyst.* 17 (3), 954–965. doi:10.1002/2015gc006120

Segall, P., and Davis, J. L. (1997). GPS applications for geodynamics and earthquake studies. *Annu. Rev. Earth Planet. Sci.* 25 (1), 301–336. doi:10.1146/annurev.earth.25.1.301

Shaanxi Earthquake Agency (1996). *Active Fault zone on the northern margin of qining mountains*. Beijing, China: Seismological Press.

Shen, X. Z., Zhou, Q. M., Cheng, S. Y., Zheng, W. J., Zhang, P. Z., Zhang, D. L., et al. (2022). Contrasting crustal structures crossing the boundary region of the southwest Ordos block and its tectonic implications revealed by dense seismic arrays. *Tectonophysics* 831, 229342. doi:10.1016/j.tecto.2022.229342

Shen, Z. K., Wang, M., Zeng, Y. H., and Wang, F. (2015). Optimal interpolation of spatially discretized geodetic data. *Bull. Seismol. Soc. Am.* 105 (4), 2117–2127. doi:10.1785/0120140247

Shentu, B. M., Song, F. M., Cao, Z. Q., and Wang, Y. P. (1991). Preliminary study on late quaternary fault scarps on the northern piedmont of qiling mountain. *Seismol. Geol.* 13 (1), 15–25.

Shi, F., Li, S., and Moreno, M. (2020). Megathrust locking and viscous mantle flow induce continental shortening in Central Andes. *Pure Appl. Geophys.* 177 (6), 2841–2852. doi:10.1007/s00024-019-02403-0

Si, X., Teng, J. W., Liu, Y. S., Ma, X. Y., Qiao, Y. H., Dong, X. P., et al. (2016). Crust structure of the Qinling orogenic and the region on its north and south margins from teleseismic receiver function. *Chin. J. Geophys.* 59 (4), 1321–1334. doi:10.6038/cjg20160414

Slemmons, D. B. (1977). Faults and earthquake magnitude". (State-of-the-art for assessing earthquake hazards in the United States). Report 24. WES. Available from: https://apps.dtic.mil/sti/citations/ADA182901.

Song, S. W., Li, Y. H., and Hao, M. (2022). Active crustal deformation model of the Fen–Wei rift zone, North China: Integration of geologic, geodetic, and stress direction datasets. *Front. Earth Sci.* 10, 964800. doi:10.3389/feart.2022.964800

Sun, J. M. (2005). Long-term fluvial archives in the Fen Wei Graben, central China, and their bearing on the tectonic history of the India–Asia collision system during the Quaternary. *Quat. Sci. Rev.* 24 (10-11), 1279–1286. doi:10.1016/j.quascirev.2004.08.018

Sun, J. M., and Xu, L. L. (2007). River terraces in the Fen Wei Graben, Central China, and the relation with the tectonic history of the India-Asia collision system during the Quaternary. *Quat. Sci.* 27 (1), 20–26. doi:10.3321/j.issn:1001-7410.2007.01.003

Sykes, L. R. (1971). Aftershock zones of great earthquakes, seismicity gaps, and earthquake prediction for Alaska and the Aleutians. *J. Geophys. Res.* 76 (32), 8021–8041. doi:10.1029/JB076i032p08021

Tapponnier, P., Peltzer, G., and Armijo, R. (1986). *On the mechanics of the collision between India and Asia*. London: Geological Society.

Tocher, D. (1958). Earthquake energy and ground breakage. *Bull. Seismol. Soc. Am.* 48 (2), 147–153. doi:10.1785/BSSA0480020147

Vigny, C., Simons, W. J. F., Abu, S., Bamphenyu, R., Satirapod, C., Choosakul, N., et al. (2005). Insight into the 2004 sumatra–andaman earthquake from GPS measurements in southeast Asia. *Nature* 436 (7048), 201–206. doi:10.1038/nature03937

Wang, C. C. (1965). On the Weihe graben. *Acta Geol. Sin.* 45, 153–164.

Wang, F., Wang, M., Wang, Y. Z., and Shen, Z. K. (2015). Earthquake potential of the Sichuan-Yunnan region, Western China. *J. Asian Earth Sci.* 107, 232–243. doi:10.1016/j.jseaes.2015.04.041

Wang, J. M. (1986). On the Fenwei rift. *J. Xi'an Colle. Geol.* 8, 36–49.

Wang, M., and Shen, Z. K. (2020). Present-day crustal deformation of continental China derived from GPS and its tectonic implications. *J. Geophys. Res. Solid Earth* 125 (2), e2019JB018774. doi:10.1029/2019JB018774

Wdowinski, S. (2009). Deep creep as a cause for the excess seismicity along the San Jacinto fault. *Nat. Geosci.* 2 (12), 882–885. doi:10.1038/ngeo684

Wells, D. L., and Coppersmith, K. J. (1994). New empirical relationships among magnitude, rupture length, rupture width, rupture area, and surface displacement. *Bull. Seismol. Soc. Am.* 84 (4), 974–1002. doi:10.1785/BSSA0840040974

Wen, X. Z., Du, F., Yi, G. X., Long, F., Fan, J., Yang, P. X., et al. (2013). Earthquake potential of the Zhaotong and Lianfeng fault zones of the eastern Sichuan-Yunnan border region. *Chin. J. Geophys.* 56 (10), 3361–3372. doi:10.6038/cjg20131012

Wen, X. Z., Fan, J., Yi, G. X., Deng, Y. W., and Long, F. (2008). A seismic gap on the Anninghe fault in Western Sichuan, China. *Sci. China Ser. D-Earth. Sci.* 51 (10), 1375–1387. doi:10.1007/s11430-008-0114-4

Wen, X. Z., Yi, G. X., and Xu, X. W. (2007). Background and precursory seismicities along and surrounding the Kunlun fault before the Ms8. 1, 2001, Kokoxili earthquake, China. *J. Asian Earth Sci.* 30 (1), 63–72. doi:10.1016/j.jseaes.2006.07.008

Wiemer, S., and Wyss, M. (1997). Mapping the frequency-magnitude distribution in asperities: An improved technique to calculate recurrence times? *J. Geophys. Res.* 102 (B7), 15115–15128. doi:10.1029/97JB00726

Williams, C. F. (1996). Temperature and the seismic/aseismic transition: Observations from the 1992 Landers earthquake. *Geophys. Res. Lett.* 23 (16), 2029–2032. doi:10.1029/96GL02066

Woessner, J., and Wiemer, S. (2005). Assessing the quality of earthquake catalogues: Estimating the magnitude of completeness and its uncertainty. *Bull. Seismol. Soc. Am.* 95 (2), 684–698. doi:10.1785/0120040007

Wu, Y. Q., Jiang, Z. S., Yang, G. H., Fang, Y., and Wang, W. X. (2009). The application and method of GPS strain calculation in whole mode using least square collocation in sphere surface. *Chin. J. Geophys.* 52 (7), 1707–1714. doi:10.3969/j.issn.0001-5733.2009.07.005

Wyss, M., Sammis, C. G., Nadeau, R. M., and Wiemer, S. (2004). Fractal dimension and b-value on creeping and locked patches of the San Andreas fault near Parkfield, California. *Bull. Seismol. Soc. Am.* 94 (2), 410–421. doi:10.1785/0120030054

Xie, Z. Q., Fang, J. A., Tian, X. T., Zhang, B. W., and Wang, X. P. (1991). The evolution of the structural stress field and analysis of the formation mechanism in the Weihe Basin. *J. Xi'an Colle. Geol.* 13 (2), 46–52.

Xie, Z. Q. (2011). Structural model of earthquake preparation in Weihe extensional basin. *J. Catastrophol.* 26 (3), 18–21. doi:10.3969/j.issn.1000-811X.2011.03.004

Xu, S., Mi, N., Xu, M., Wang, L., Li, H., and Yu, D. (2014). Crustal structures of the Weihe graben and its surroundings from receiver functions. *Sci. China Earth Sci.* 57 (2), 372–378. doi:10.1007/s11430-013-4719-x

Xu, X., Han, Z., and Yang, X. (2016). *Seismotectonic Map of China and its adjacent regions*. Beijing: Seismological Press.

Xu, X. W. (2006). Active faults, associated earthquake disaster distribution and policy for disaster reduction. *Technol. Earthq. Disaster Prev.* 1 (1), 7–14. doi:10.3969/j.issn.1673-5722.2006.01.002

Yang, Q. H. (2022). *Research on the seismic activity history of faults in the northern margin of Qinling Mountains based on structural geomorphological features*. Xi'an, China: Chang'an University.

Yi, G. X., Wen, X. Z., Wang, S. W., Long, F., and Fan, J. (2006). Study on fault sliding behaviors and strong-earthquake risk of the Longmenshan-Minshan fault zones from current seismicity parameters. *Earthq. Res. China* 22 (2), 117–125. doi:10.3969/j.issn.1001-4683.2006.02.001

Yin, H. Q., Guo, X. Y., Chang, M., Zhan, W., Li, L. Y., and Xu, D. Z. (2020). Inversion of seismic hazard of the Xianshuihe fault by cross-fault and GPS crustal deformation data. *Acta Geol. Sin.* 94 (8), 2487–2499. doi:10.19762/j.cnki.dizhixuebao.2020055

Yu, Z., Shen, X., Liang, H., Zheng, W., and Liu, X. (2022). The characteristics of major faults and stress field in Weihe -- Yuncheng basin constrained by seismic activity and focal mechanism solutions. *Seismol. Geol.* (2), 395–413. doi:10.3969/j.issn.0253-4967.2022.02.008

Zhang, A. L., Chong, J., and Mi, F. S. (1990). A paleoseismological profile across piedmont fault zone at Taipingkou on northern segment of Qinling Mountains. *Seismol. Geol.* 12 (4), 333–334.

Zhang, A. L., Chong, J., and Mi, F. S. (1991). *Late quaternary activity characteristics of the fault zone in the northern margin of qinling mountains and its paleoearthquakes*. Beijing, China: Seismological Press.

Zhang, E. H., Shi, Y. Q., Zhang, Y., Li, M., Li, G. Y., Pei, H. D., et al. (2021). Extension and structural feature of the buried segment of Taochuan–Huxian Fault in the Weihe Basin. *Seismol. Geol.* 43 (6), 1485–1506. doi:10.3969/j.issn.0253-4967.2021.06.008

Zhang, P. Z., Deng, Q. D., Zhang, Z. Q., and Li, H. B. (2013). Active faults, earthquake hazards and associated geodynamic processes in continental China. *Sci. Sin. Terrae* 43 (10), 1607–1620. CNKI:SUN:JDXK.0.2013-10-005. doi:10.1360/zd-2013-43-10-1607

Zhang, P. Z., Wang, M., and Gan, W. J. (2003). Slip rates along major active faults from GPS measurements and constraints on contemporary continental tectonics. *Earth Sci. Front.* 10 (U08), 81–92. doi:10.3321/j.issn:1005-2321.2003.z1.014

Zhang, P. Z., Zheng, D. W., Yin, G. M., Yuan, D. Y., Zhang, G. L., Li, C. Y., et al. (2006). Discussion on late Cenozoic growth and rise of northeastern margin of the Tibetan Plateau. *Quat. Sci.* 26 (1), 5–13. doi:10.3321/j.issn:1001-7410.2006.01.002

Zhang, X., Jiang, Z. S., and Zhang, S. X. (1998). Whole calculation of the crustal visual strain field with the least square collocation. *Crustal Deform. Earthq.* 18 (2), 57–62.

Zhang, Y. Q., Dong, S. W., Wang, H. Y., Feng, M., Thybo, H., Li, J. H., et al. (2022). Coupled lithospheric deformation in the qinling orogen, central China: Insights from seismic reflection and surface-wave tomography. *Geophys. Res. Lett.* 49 (14). doi:10.1029/2022GL097760

Zhang, Y. Q., Vergély, P., and Mercier, J. L. (1999). Pliocene-Quaternary faulting pattern and left-slip propagation tectonics in North China. *J. Geomechan.* 5 (3), 40–46. doi:10.3969/j.issn.1006-6616.1999.03.007

Zhang, Y. Q., Ma, Y. S., Yang, N., Zhang, H. P., and Shi, W. (2005). Late Cenozoic left-slip faulting process of the east Kunlun-Qinling fault system in West Qinling region and its eastward propagation. *Acta Geosci. Sin.* 26 (1), 1–8. doi:10.3321/j.issn:1006-3021.2005.01.001

Zhang, Y. Q., Mercier, J. L., and Vergély, P. (1998). Extension in the graben systems around the Ordos (China), and its contribution to the extrusion tectonics of south China with respect to Gobi-Mongolia. *Tectonophysics* 285 (1-2), 41–75. doi:10.1016/S0040-1951(97)00170-4

Zhang, Y. Q., Shi, W., and Dong, S. W. (2019). Neotectonics of North China: Interplay between far-field effect of India-eurasia collision and pacific subduction related deep-seated mantle upwelling. *Acta Geol. Sin.* 93 (5), 971–1001. CNKI:SUN:DZXE.10.2019-05-001. doi:10.3969/j.issn.0001-5717.2019.05.001

Zhang, Y. Q., Vergély, P., and Mercier, J. L. (1995). Active faulting in and along the Qinling Range (China) inferred from SPOT imagery analysis and extrusion tectonics of south China. *Tectonophysics* 243 (1-2), 69–95. doi:10.1016/0040-1951(94)00192-C

Zhou, Y. J., Yue, H., Zhou, S. Y., Fang, L. H., Zhou, Y., Xu, L. S., et al. (2022). Microseismicity along xiaojiang fault zone (southeastern Tibetan plateau) and the characterization of interseismic fault behavior. *Tectonophysics* 833 (20), 229364. doi:10.1016/j.tecto.2022.229364

Zhu, H., and Huang, J. (2022). Spatiotemporal aftershock evolution of the 2014 M 6.4 and 5.9 kangding double shocks in sichuan, southwestern China. *Seismol. Soc. Am.* 93 (5), 2625–2639. doi:10.1785/0220220039